

# Electronic Devices Based on Two-Dimensional Quantum Materials

Author: David Valero

*Facultat de Física, Universitat de Barcelona, Diagonal 645, 08028 Barcelona, Spain.*

Tutors: Marius V. Costache, Juan F. Sierra (Catalan Institute of Nanoscience and Nanotechnology)

**Abstract:** One of the central problems in graphene spintronics is the efficient injection and detection of spins in mesoscopic devices. To date, most of the studies in graphene spin devices use spin-sensitive contacts of Cobalt for injection and detection. However, due to its magnetic properties, Cobalt is prone to form magnetic domains and inhomogeneities, which makes it hard to control its magnetization orientation. This memoir presents a novel approach for spin injection and detection in graphene by material engineering of the ferromagnetic contacts. We have fabricated spin injector/detector contacts of a bilayer of Cobalt and Permalloy (NiFe). Our results demonstrate that Permalloy softens the magnetization reversal of the Cobalt/Permalloy bilayer while the insertion of a very thin layer of the Cobalt layer is essential for efficient spin injection/detection into graphene.

## I. INTRODUCTION

Contrary to electronics, in which electron current flow is manipulated in electronic devices, spin-based electronics or spintronics aims to take advantage of the electron spin degree of freedom in order to transport and manipulate information. Spin devices rely on three key fundamental concepts: spin injection, detection, and manipulation. First generation of spin devices were based on normal metals, such as aluminum and copper used as spin transport channels [8]. The recent discovery and isolation of different two-dimensional (2D) materials have provided a very rich platform to study spin physics as well as the development of prototypical devices reaching the atomically thin limit. Among 2D materials, graphene, an atomically thin layer of carbon atoms arranged in a honeycomb crystal lattice, is the most prominent example. Due to its low spin-orbit coupling and lack of hyperfine interaction, graphene is one of the best materials for spin transport with spin communication over distances as large as a few micrometers [6]. Besides, it is a gate-tunable material, *i.e.* its carrier density can be controlled by electrostatic gating, with extremely high carrier mobilities [6, 7]. All these unique physical properties offer unprecedented opportunities for the development of graphene-based spin logic devices with high-speed operation rates and low-power consumption. One of the central problems in the development of graphene spin devices is to engineer efficient spin injection/detection contacts as well as to find routes for spin control and manipulation [7]. Spin injection/detection is realized by attaching ferromagnetic (FM) contacts to graphene, since when a current is applied through them, it becomes spin polarized [3]. To date, the most efficient FM element for spin injection/detection in graphene is cobalt, Co. However, due to its magnetic properties, it is prone to form magnetic domains which disrupt the spin injection/detection and results in troublesome effects. One of the most common issue is the nucleation, propagation and pinning of magnetic domains within the contacts, preventing them from a coherent magnetization reversal under an external

magnetic field. Additionally, FMs cannot inject spin efficiently when in direct contact with graphene due to the conductivity mismatch between the two materials. To mitigate this problem, tunnel barriers are intercalated between the FM and graphene.

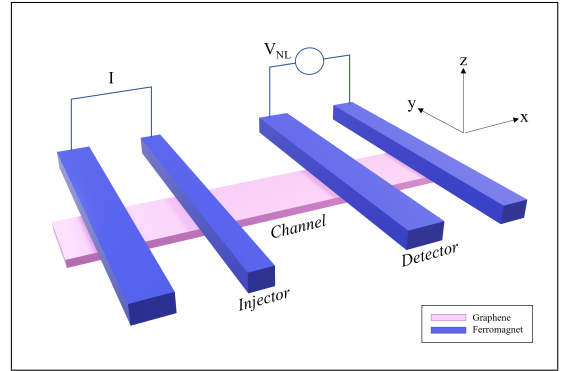


FIG. 1: Non-local configuration in lateral devices. The channel used in this work is graphene, and the injector (FM1) and detector (FM2) have to be FM in order to be spin-sensitive.  $\hat{x}$  is defined parallel to the graphene channel;  $\hat{y}$  parallel to the contacts and  $\hat{z}$  perpendicular to the graphene plane.

This work presents an attempt to engineer spin injectors and detectors with softer magnetization properties compatible with graphene. We have chosen Permalloy (Py), a magnetic alloy made of Fe and Ni (in the proportion Ni<sub>50</sub>Fe<sub>50</sub> in this work) as soft FM material in combination with very thin layers (3 to 5 nm) of Co. While the spin injection/detection efficiency is driven by the thin layer of Co, an upper thick layer of Py is expected to provide a cleaner magnetization reversal of Co, hence getting rid of pinned magnetic domains and imprinting softer properties by proximity effects. In this work, I have fabricated graphene-based lateral spin devices and measured their spin transport properties using conventional Co/TiO<sub>x</sub> contacts as well as a new layout based on Py/Co/TiO<sub>x</sub> spin injectors and detectors. Particularly, I have characterized these devices using non-local detection techniques, enabling to measure spin valve effects

and spin precession in graphene at room temperature.

## II. THEORETICAL BACKGROUND

### A. Spin Injection and Detection

Spin injection and detection is achieved by attaching spin-sensitive contacts, in this case metal FMs, to a non-magnetic (NM) material, which acts as spin channel. The non-local lateral device, central to this work, is then composed of a NM channel material, *i.e.* graphene, through which spins diffuse, and four planar FM contacts attached to it, with the two FM probes (FM1 and FM2) in the middle acting as spin injector and detector (Fig. 1).

Owing to the different spin populations and mobilities of spin-up and spin-down electrons in FM materials, a charge current  $I$  running through the FM injector becomes spin-polarized. When  $I$  runs from the FM injector towards the graphene spin channel, which is non-magnetic (NM) and hence, its spin populations are equal, a non-equilibrium spin accumulation beneath the FM contact is built, whose magnitude is quantified by a splitting  $\Delta\mu = (\mu_{\uparrow} - \mu_{\downarrow})$  in the spin-dependent electrochemical potentials  $\mu_{\uparrow}$  and  $\mu_{\downarrow}$  of the spin channel.

These accumulated spins then diffuse in both directions away from the injection point over a characteristic distance  $\lambda_{sf}$ , called spin diffusion length. Due to the non-local detection scheme, in the direction of the detector a pure spin current flows since the charge current is not circulating across this region. If the detector contact is within the spin diffusion length ( $L < \lambda_{sf}$ , with  $L$  the spin channel length), its Fermi level tends to equilibrate closer to the local  $\mu_{\uparrow}$  or  $\mu_{\downarrow}$  depending on its magnetization orientation. Pure spin currents can be then detected as a voltage signal  $V_{nl} = P_i \cdot P_d \cdot \Delta\mu / 2e$ , where  $P_i$ ,  $P_d$  are the spin polarization of the injector and detector respectively and  $e$  is the elementary charge unit. The non-local signal is often converted in units of resistance defined as  $R_{nl} = V_{nl}/I$ , whose value is then  $R_{nl} \propto P_i P_d$ . Note that this is not a common resistance definition because its values can be negative depending on the relative magnetization orientation of the injector/detector.

When the spin channel resistance is higher than that of the FM injector, as is the case of system comprising FM contacts in a planar contact geometry with graphene, the spin injection efficiency is low and the spins are partially lost due to the spin absorption in the FM, resulting in a low spin polarization value. This problem can be nevertheless circumvented by introducing a thin insulating barrier that facilitates tunneling spin injection [3], hence increasing the injection efficiency and reducing undesired contact-induced spin absorption effects.

Spin diffusion along the spin channel can be described by the diffusive transport model derived from the Boltzmann equation  $\nabla^2 \Delta\mu = (1/\lambda)^2 \Delta\mu$ , whose solution in the

1D approximation is  $\Delta\mu = \mu_0 e^{-\frac{\lambda_{sf}}{x}}$ , where  $\mu_0 = \mu_{\uparrow} - \mu_{\downarrow}$  at the injection point, *i.e.*  $x=0$ .

As the electrochemical potential decays exponentially, the outer detector contact will barely detect any spin signal, and can be defined as 0. The measured  $V_{nl}$  at the detection region depends on the relative magnetization orientation of the FM injector and the detector, which can be controlled by an external magnetic field to generate parallel (PA) or anti-parallel (AP) states.

### B. Spin valve effect

The relative magnetization orientation of the injector and detector contacts is achieved by taking advantage of their magnetic shape anisotropy. As discussed in [4], if the FM does not have a strong crystal anisotropy – *i.e.* the crystal structure drives the magnetization direction – the magnetization will be oriented in the direction that minimizes the shape anisotropy energy. Minimizing this energy can also be seen as the material avoiding surface magnetic charge accumulation, hence, orienting the magnetization in the "easy axis" or, in other words, along the long-axis of the FM. Considering this concept, the injector and detector are designed with a well-defined long-axis, in this case along the  $\hat{y}$  direction (Fig. 1). The injector and detector contacts can then be in four different configurations depending on their magnetization orientations, two of them PA ( $\uparrow\uparrow, \downarrow\downarrow$ ) and two AP ( $\downarrow\uparrow, \uparrow\downarrow$ ), where  $\uparrow$  is defined as  $+\hat{y}$  and  $\downarrow$  as  $-\hat{y}$ . When changing from one state to another  $V_{nl}$  changes its value and sign, resulting a square and sharp signal. The magnitude of this change is typically expressed in terms of resistance units  $\Delta R_{NL} = R_{nl}^{\uparrow\uparrow} - R_{nl}^{\downarrow\downarrow}$ , and is called spin valve signal.

In order to control PA and AP states, the injector and detector need to have slightly different coercive fields  $H_C$ . As  $H_C$  depends on the geometry of the magnet, the contacts have been designed with different widths. If an external magnetic field  $B_y$  is applied in  $\hat{y}$  (from now on, in plane field 'IP'), making backward and forward field sweeps will result in a non local spin signal with well defined levels of opposite sign for the PA and AP states.

### C. Hanle spin precession

Another key measurement to determine the spin related parameters in the system is spin precession experiments, in which an external magnetic field is applied out of the graphene plane (OP field). This spin precession measurements have four different contributions [6]:

**Spin precession:** Spin diffusing from the injector to the detector rotates in the graphene plane with a Larmor frequency that depends on the magnitude of the OP field  $\omega = \frac{g\mu_B}{\hbar} B_{\perp}$ , where  $g$  is the electronic g-factor of the medium,  $\mu_B$  is the Bohr magneton and  $\hbar$  is the reduced

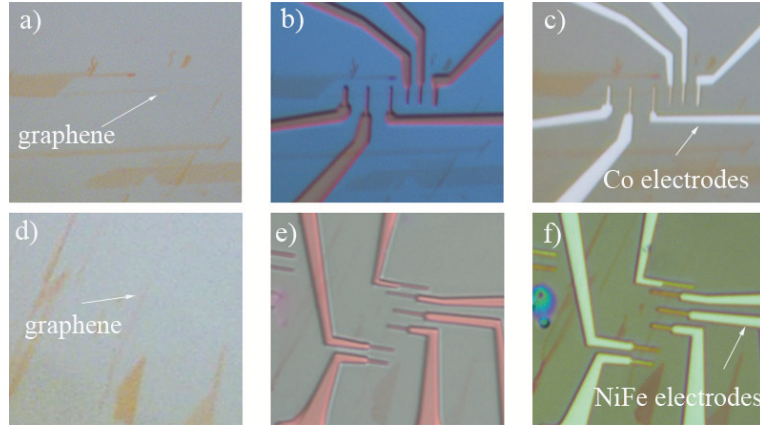


FIG. 2: Optical images of lateral spin device, device D1 (first row) and device D2 (second row), taken during the fabrication process. a) and d) show the exfoliated graphene flakes. b) and e) show the polymer masks made using EBL process. c) and f) show the ready to measure devices after the metal deposition.

Planck constant. This results in an oscillatory signal that goes as  $\cos(\omega t)$ .

**Spin diffusion:** As previously explained, spins transport in the graphene channel is a diffusive process with a signal that decays exponentially from the injection point. This contribution is reflected in the distribution function:  $f(t) = \frac{1}{\sqrt{4\pi Dt}} e^{-L^2/4Dt}$ , where  $D$  stands for the spin diffusion constant.

**Spin dephasing:** While diffusing, spins might scatter with impurities and flip their spin orientation. This contribution is given by the expression  $e^{-t/\tau_s}$ , where  $\tau_s$  is the spin lifetime. The resulting expression for the spin precession signal is given by

$$V_{\text{nl}}(B) = \pm \frac{I_{P_s} P_d}{e^2 N A} \int_0^\infty \frac{1}{\sqrt{4\pi D_s t}} \exp\left[-\frac{L^2}{4D_s t}\right] \cos(\omega_L t) \exp(-t/\tau_s) dt, \quad (1)$$

where the sign  $+$  ( $-$ ) accounts for the PA (AP) magnetization configuration of the injector/detector, and  $N$  and  $A$  are the density of states at the Fermi energy and the contact area, respectively.  $D$  and  $\tau_s$  are related by the expression  $\lambda = \sqrt{D_s \tau_s}$ .

### III. DEVICE FABRICATION PROCESS

The basic steps in the device fabrication are described below. An schematic of this steps can be found in Appendix A.

**Mechanical exfoliation of graphene.** We start by the mechanical exfoliation of graphene from a highly-oriented pyrolytic graphite (HOPG) source on a 440 nm of  $\text{SiO}_2$  substrate. Here, the aim is to obtain long enough flakes with dimensions of about 20  $\mu\text{m}$  long and 1  $\mu\text{m}$  wide. The exfoliation follows the standard 'scotch tape method', in which an adhesive tape is stuck on top of the HOPG. Large areas of graphite are adhered to the tape and subsequently peeled-off. The tape is then stuck to the  $\text{Si}/\text{SiO}_2$  substrate, which has been previously cleaned

with an oxygen plasma. The transferred flakes are then inspected under an optical microscope in the bright field mode. Single layers of graphene with the required geometry are identified by optical contrast (Fig. 2a, d), which has been previously calibrated by Raman spectroscopy, and selected for the fabrication of spin devices.

**Device design and electron beam lithography (EBL).** The design of devices have been done using the software K-Layout. The FM contacts are defined using EBL. First, the chip is coated with a bilayer polymer of Methyl methacrylate (MMA) and Poly(methyl methacrylate) (PMMA). This mask is then exposed to an e-beam, that defines the contact dimensions previously designed. This exposure changes the chemical properties of the exposed areas, making it soluble in methyl-isobutyl-ketone:isopropanol (MIBK:IPA). Once this chemical developing is made, the remaining polymer acts as a mask with the shape of our device (Fig. 2b, e).

**Tunnel Barriers formation and contact deposition.** Next, the chip is placed in an ultra high vacuum (UHV) metal deposition chamber, where the metal contacts and the tunnel barriers are deposited via e-beam evaporation. We have evaporated two types of contacts which define the two studied spin devices, D1 and D2. The contacts are made by two core elements; tunnel barriers and ferromagnetic materials. For the fabrication of the former we have used  $\text{TiO}_2$  in both D1 and D2 with slightly different thicknesses. The barrier fabrication consists on depositing 4  $\text{\AA}$  for D1 and 5  $\text{\AA}$  for D2 of Ti which is then oxidize *in-situ* at a pressure of 0.017 atm for 30 min. In order to obtain a better quality of the barriers we have made this process twice. Once tunnel barriers are fabricated, we deposit the ferromagnetic material that will define the spin polarization and magnetization behavior of the device contacts. In the case of D1 we have used 30 nm of Co, whereas D2 consists of 4 nm of Co and 27 nm of Py. After the evaporation of FM materials we have evaporated a 3 nm capping layer of Al

	L ( $\mu\text{m}$ ) $\pm 0.2$	W ( $\mu\text{m}$ ) $\pm 0.2$	W <sub>i</sub> ( $\mu\text{m}$ ) $\pm 0.01$	W <sub>d</sub> ( $\mu\text{m}$ ) $\pm 0.01$	V <sub>CNP</sub> (V) $\pm 0.5$	$\mu$ (cm <sup>2</sup> /Vs) $\pm 50$
D1	3.9	0.6	0.45	0.24	-19.0	5860
D2	2.4	0.6	0.17	0.13	-6.0	3700

TABLE I: Characteristics of the graphene channels and contacts of D1 and D2. From left to right: Graphene channel length L and width W, widths of injector W<sub>i</sub> and detector W<sub>d</sub>, charge neutrality point or Dirac point position V<sub>CNP</sub> and mobility of the channel  $\mu$  (For the mobility calculation, see Appendix C).

to prevent oxidation. Finally, the chip is rinsed in acetone to lift-off the polymer, to be subsequently cleaned with isopropanol and dried up with a flux of N<sub>2</sub> gas (Fig. 2c, f). The chip is placed onto a chip carrier. The electrical connections have been done using a wire bonding technique.

**Electrical measurements.** The chip carrier is installed into a vacuum cryostat that can be rotated, thus enabling to change the direction of the applied magnetic field with respect to the chip surface, which is essential to measure both spin valve and spin precession magnetic field configurations without taking the chip out of the cryostat. We have used a current source in delta mode configuration to avoid thermal contributions to the measurements, and measured the voltage in a triggered Keithley nanovoltmeter. The magnetic field is created by a Lakeshore electromagnet.

#### IV. RESULTS

Here the results of the measurements for D1 and D2 are presented and then discussed. Prior to the spin valve and spin precession measurements, the resistance vs. gate voltage dependence for the graphene channel was measured. The back-gate voltage, which is applied to the P-doped region of the Si substrate, enables to shift the graphene Fermi level and control what type of carriers (electron or holes) dominate the transport. By applying positive gate voltages, the graphene becomes n-doped (electron doped), while applying negative voltages makes graphene p-doped (hole doped). As shown in Fig. 3, the resistance reaches a maximum (values in Table I) called the Dirac point or charge neutrality point (CNP). At this maximum the graphene carrier density equals zero, whose value increases away from it (see Appendix B). We have studied the gate-dependent resistance of our devices in the range from +30 V to -30 V.

After the electrical characterization of graphene, we have carried out spin valve and spin precession measurements using the non-local configuration scheme presented above. Figures 4a and 4c show the spin valve effect for D1 and D2, respectively, with spin signals  $\Delta R_{NL}^{D1} = 300 \pm 20$  m $\Omega$  for D1 and  $800 \pm 20$  m $\Omega$  for D2. Besides the magnitude of the spin signal, there are several differences between the spin signal behavior measured in the two spin devices. On one hand, D2 shows several switching states or steps. We interpret such additional steps in the spin signal as an indication of the different magnetic configurations of all the FM contacts as illustrated by the arrows in Fig. 4c. On the other hand, D1 (Fig. 4a) shows only

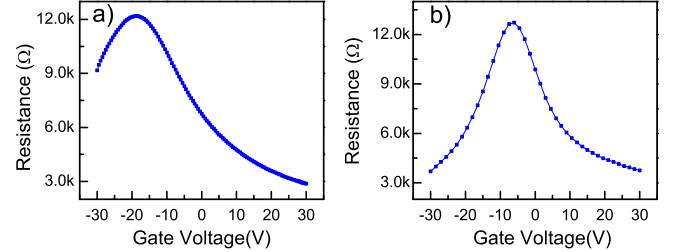


FIG. 3: Gate voltage dependence of the resistance of the graphene channel for a) D1 and b) D2. The measurements are made in 4 terminal configuration. This is, applying current through the external contacts and measuring voltage between the internal ones. The error bars size is smaller than the dot's size.

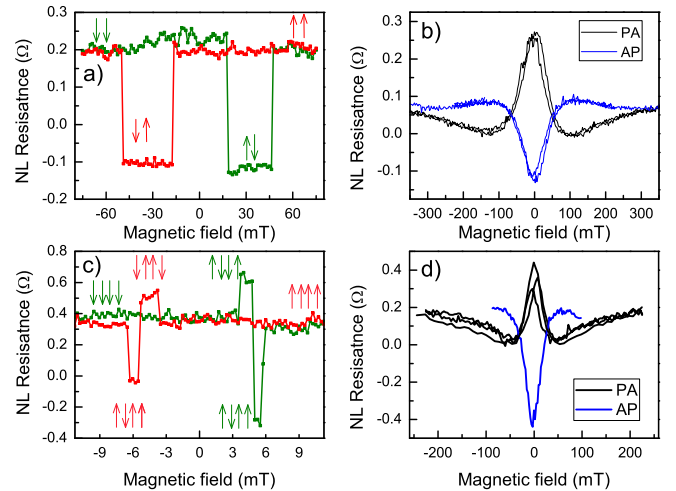


FIG. 4: Measurements in non local configuration at  $V_G = 30$  V. a) Spin valve and b) Hanle spin precession of D1. c) Spin valve and d) Hanle spin precession of D2. In a) c), the magnetic field was swept from positive to negative values (red line) and vice versa (green line). Vertical arrows show the magnetization direction of the contacts in each region. In a), only the magnetization direction of the injector-detector are taken in count, given that there are not external switchings. In c) all the contacts are taken in count and there are displayed in the same order as in Fig. 1. b) and d) show the parallel (black line) and anti-parallel (blue line) states of the spin precession signal. The error bars size is smaller than the point's size.

rations of all the FM contacts as illustrated by the arrows in Fig. 4c. On the other hand, D1 (Fig. 4a) shows only

two well-defined states that corresponds to the two relative magnetization orientation, *i.e.* PA and AP, of the FM injector and detector. Contrary to D2, here the magnetization reversal of the outer FM contacts are not detected because they are very far away and their switching have no influence in the spin signal detected in the inner FM. In addition, we have observed that switching fields in D2 are much smaller than in D1. One should expect a lower switching field for wider contacts. However, this is in stark contrast when comparing the switching fields and contacts widths of D1 and D2 (see Table I). Such switching behavior is due to the different composition of FM contacts in D1 and D2. While FM contacts in D1 are made of pure Co, the contacts of D2 are made of a much softer bilayer of Py/Co. It is well known that Py is magnetically softer than Co, so that its coercive field is lower. We believe that the thick Py layer is driving the switching behavior of the thin Co layer in D2, enabling to switch the magnetization of FM contacts at lower magnetic fields than in D1.

Figures 4b and 4d show the spin precession measurements in D1 and D2, respectively. As in the commonly used FM contacts like the ones in D1, we have achieved a clear spin precession signal in D2 using 4 nm of Co, followed by 27 nm of Py. It is worth to note that this FM contact composition has been studied for the first time during this work. Previous attempts carried out by other researchers at the host group in the past using pure Py contacts without the intercalation of the Co thin layer have been demonstrated not to be efficient for spin injection and detection in graphene [2]. These experimental facts make us think that, while the efficiency of the spin injection and detection is driven by the FM in contact with graphene, being Co the most suitable material compatible with graphene, its magnetization properties can be improved by an adjacent layer of a softer magnetic materials, as Py.

## V. CONCLUSIONS

Within the frame of my final degree thesis, we have demonstrated efficient injection, propagation and detection of spin in graphene by developing novel spin-sensitive contacts based on the combination of thin layers of Co, acting as spin polarizers, together with Py, that soften the overall magnetic properties of the contacts. The measured signals in Cobalt/Permalloy devices are comparable with the signal obtained on standard devices based on pure Cobalt contacts. This result demonstrates the dominant role of Cobalt for spin injection and detection. Importantly, in Cobalt/Permalloy-based devices the switching of the ferromagnetic electrodes takes place on a smaller magnetic field range compared with Cobalt-based devices, demonstrating the role of Permalloy in controlling the reversal or switching of the ferromagnetic electrodes. Finally, these results could help to design future spintronic devices properties. In particular, by removing undesired magnetic domain wall formation or related non-homogeneous magnetic textures in the contacts attached to the active spin device.

## Acknowledgments

I would like to thank my family and friends for following and supporting my research as enthusiastically as I do. Especially, I want to thank Marius V. Costache and Juan F. Sierra for their excellent labour as tutors and for their patience and dedication. I would also like to thank to Prof. Sergio O. Valenzuela for allowing me to do my TFG in his group. Lastly, I want to thank all the Physics and Engineering of Nanodevices group of ICN2 for kindly integrating me in their research, as well as for supporting me during all this project.

- 
- [1] Neumann, I., O. Valenzuela, S. (2014). "Electronic Spin Transport and Thermoelectric Effects in Graphene" (Doctoral dissertation, Catalan Institute of Nanoscience and Nanotechnology, Bellaterra, Spain). Retrieved from <https://digital.csic.es/handle/10261/122565>
  - [2] Urgell, C., O. Valenzuela, S. (2016). "Interface & Contact Engineering in Graphene Spintronic Devices" (Unpublished master's thesis, Catalan Institute of Nanoscience and Nanotechnology, Bellaterra, Spain).
  - [3] Žutić, Igor. Fabian, Jaroslav. Das Sarma, S. "Spintronics: Fundamentals and applications". Reviews of Modern Physics. Vol. **76**, 323 (April 2004).
  - [4] Xiaobin, W. "Magnetization Dynamics Symmetry in Spin Torque Induced Magnetization Switching". Symmetry **2**, 1000-1001 (1-6-2010).
  - [5] Fan, X., Zhou, H., Rao, J., Zhao, X., Zhao, J., Zhang, F., Xue, D. "Magnetic field-dependent shape anisotropy in small patterned films studied using rotating magnetoresistance". Sci Rep **5**, 16139 (2015).
  - [6] Han, W., Kawakami, R.K., Gmitra, M., Fabian, J. "Graphene spintronics". Nature Nanotech **9**, 794-807 (2014).
  - [7] Sierra, J.F., Fabian, J., Kawakami, R.K., Roche, S., O. Valenzuela, S. "Van der Waals heterostructures for spintronics and opto-spintronics". Nature Nanotech **16**, 856-868 (2021).
  - [8] Costache, M. V., Zaffalon, M., van Wees, B. J. "Spin accumulation probed in multiterminal lateral all-metallic devices". Phys. Rev. B **74**, 012412 (31-7-2006).

## VI. APPENDIX

## A. Device Fabrication Schematic

Fig. 5 illustrates the device fabrication process explained in Section III.

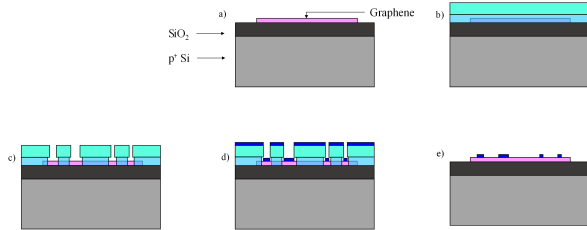


FIG. 5: Schematic of the steps followed in the device fabrication. a) Exfoliation. b) Polymer coating and e-beam exposition. c) Polymer developing. d) Contact deposition. e) Lift-off.

## B. Carrier density of Graphene vs. Gate Voltage

The p-doped Si and graphene act as capacitor plates, separated by 440 nm of SiO<sub>2</sub>.

$$C = \frac{Q}{U} = \frac{eN}{V_G}$$

Where  $e$  is the elementary charge,  $V_G$  is the applied gate voltage and  $N$  is the number of carriers. Also, the capacity of a 2D capacitance is  $C_{Di\text{el}} = \frac{\epsilon_0 \epsilon_r}{d} A$ .

Combining this, we can express the carrier density of graphene as a function of the applied gate voltage:

$$n = \frac{N}{A} = \frac{\epsilon_0 \epsilon_r}{de} (V_G - V_{CNP}) = \alpha (V_G - V_{CNP}) \quad (2)$$

A shift in voltage has to be implemented in order to fulfil  $n = 0$  at the charge neutrality point (CNP).

From [1] (p. 27) we extract the proportionality constant for 440 nm of SiO<sub>2</sub>  $\alpha = 49 \cdot 10^9 V^{-1} s^{-1}$ . Having this, we can express carrier density vs. voltage as in Fig.6. Note that negative carrier densities don't have physical

sense, for that reason in Fig.6 the results are shown in absolute value. Left of the CNP shows hole carrier density, and on the right, electron carrier density.

## C. Mobility

Knowing the resistance (since in 2D,  $\sigma = \rho^{-1} = \frac{L}{RW}$ ) and carrier density dependence with the applied gate

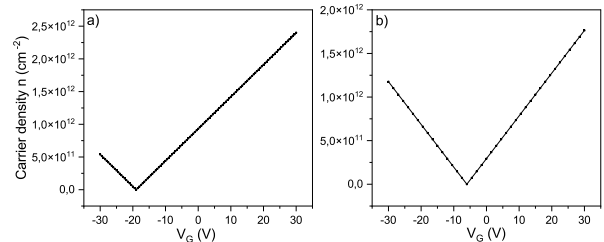


FIG. 6: Carrier density of as a function of the gate voltage. Note that at the charge neutrality point of each device a) D1,  $V_{CNP} = -19$  V b) D2,  $V_{CNP} = -6$  V, the carrier density is 0.

voltage, we can calculate the mobility as:

$$\mu = \frac{\sigma(V_G)}{en(V_G)} \quad (3)$$

Ideally, mobility should be a constant value with a Dirac delta at  $n = 0$ . In Fig. 7, the mobility value can be estimated with the converged values far from the divergence zone.

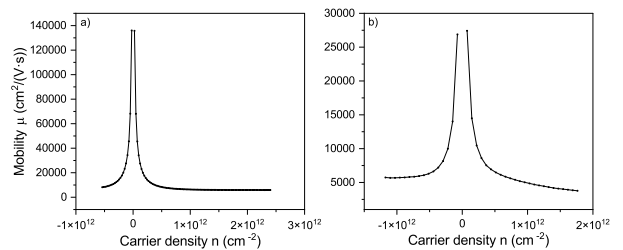


FIG. 7: Graphical representation of the mobility of a) D1 and b) D2 vs. carrier density, calculated following eq. 3. Mobility value is extracted from  $n \geq 2 \cdot 10^{12} \text{ cm}^{-2}$ , where it starts to converge.